

Elemental substitution – often referred to as doping when done with small amounts of substitutional elements – is the most commonly utilized strategy to overcome these problems. The most thoroughly investigated elements are cobalt,¹⁰ manganese¹¹ and aluminum,¹² followed by titanium¹³ and magnesium.¹⁴ These are “regular” dopants, in the sense that they were shown to enter the bulk of LNO particles,⁴ yet recently the utility of Co and Mn has been questioned.¹⁵ On the other hand, results on doping/substitution with heavier elements such as tungsten^{16,17} and zirconium¹⁸ demonstrated that even very low molar contents of foreign elements (≈ 1 mol%) can have profound consequences.⁴ These can be regarded as “surface” dopants, in that they were shown to have little solubility in the bulk of LNO, but they are able to significantly modify the surface structure of the material (yet, they penetrate into the LNO CAM to some extent, as opposed to a coating strategy).

Among the elements that were initially reported to be promising, gallium has been neglected and lacks detailed investigation. In fact, despite an encouraging seminal work of Nishida *et al.*,¹⁹ the number of studies on Ga doping remained limited.^{20–22} According to these reports, Ga doping leads to improved electrochemical performance of LNO, with an optimal Ga fraction of 2 or 2.5 mol%. Gallium is assumed to be localized on the Ni sites and to stabilize the layered structure during electrochemical cycling, although structural investigations are entirely missing in the literature, at both the bulk and surface level. The location of gallium in the crystal structure of LNO and thus the true nature of its stabilizing effect is not trivial in terms of steric considerations. Gallium, which is likely included as Ga^{3+} , has a significantly larger ionic radius [$r(\text{Ga}^{3+}) = 0.62 \text{ \AA}$]²³ than trivalent nickel [$r(\text{Ni}^{3+}) = 0.56 \text{ \AA}$].²³ While Al^{3+} and Co^{3+} are smaller than both monovalent lithium [$r(\text{Li}^+) = 0.76 \text{ \AA}$]²³ and Ni^{3+} and thus certainly occupy the Ni sites, that is not the case for Ga^{3+} , which can in principle occupy both available cation sites. For steric reasons, one may also expect Ga^{3+} to compete for site occupancy with Ni^{2+} [$r(\text{Ni}^{2+}) = 0.69 \text{ \AA}$],²³ resulting from LNO's off-stoichiometry.

In this work we aim at filling the gap of structural information on the Ga doping of LNO. The substitution strategy is revisited to complement and update previous findings by systematic investigation of its effects on the structure and electrochemical properties of LNO. In addition, insight into the structural degradation upon electrochemical cycling is provided.

Experimental section

Synthesis

We initially assumed a stoichiometry $\text{LiNi}_{1-y}\text{Ga}_y\text{O}_2$ ($0.00 \leq y \leq 0.05$, referred to as LNO with 0 to 5% nominal doping). Samples were synthesized from suitable amounts of $\text{Ni}(\text{OH})_2$ (BASF SE), $\text{LiOH}\cdot\text{H}_2\text{O}$ (BASF SE) (with $n(\text{Ni} + \text{Ga}):n(\text{Li}) = 1:1.01$), and $\text{Ga}(\text{NO}_3)_3\cdot x\text{H}_2\text{O}$ (99.9%, Sigma Aldrich). An aqueous solution of the Ga precursor was prepared and added to the mixture of Ni and Li hydroxides (typically 2.5 ml deionized water per 10 g of total precursor mass). The resulting suspension was

annealed at 300 °C in an Ar flow for 15 h and homogenized in a mortar before calcination in an O_2 flow at 700 °C for 10 h.

Electron microscopy

Scanning electron microscopy (SEM) and energy-dispersive X-ray spectroscopy (EDX) were carried out at 10 kV using a LEO-1530 electron microscope (Carl Zeiss AG) with a field emission source. Scanning transmission electron microscopy (STEM) of pristine and cycled (after 2 and 100 cycles) electrodes was conducted using a FEI Titan 80-300 microscope at an accelerating voltage of 300 kV. Elemental mapping was facilitated by a Tecnai G2 TEM setup equipped with an EDAX EDX detector at 200 kV. The cycled cathodes were recovered from the cells in their discharged (lithiated) state (3.0 V vs. Li^+/Li) and washed with 10 ml dimethyl carbonate (>99.0%, Sigma Aldrich) before drying and transferring them into the microscope under an inert atmosphere. Samples for TEM investigation were prepared using a focused Ga ion beam (FIB) in a STRATA-Dual Beam instrument at an accelerating voltage of 30 kV. For final polishing, the voltage was set to 2 kV. NiO (>99.99%, Sigma Aldrich) powder samples were used as comparing specimens to distinguish between the Ga content of the investigated doped samples and the Ga content stemming from the FIB specimen preparation.

Elemental analysis

The Ga, Ni and Li content of the calcination products was determined *via* inductively coupled plasma-optical emission spectroscopy (ICP-OES) using a Thermo Fischer Scientific iCAP 7600 DUO. To this end, the powder samples were dissolved using acid in a graphite furnace, and the mass fraction was determined from three independent measurements.

Thermogravimetric analysis

The water content of $\text{Ga}(\text{NO}_3)_3\cdot x\text{H}_2\text{O}$ was determined using a Netzsch TG 209F1 Libra. Powder samples were heated under an Ar flow to 600 °C at a rate of 0.5 °C min^{-1} while concurrently measuring the mass loss.

Structural characterization

The synchrotron-based XRD experiments were carried out on the MSPD beamline of the ALBA synchrotron.²⁴ Powder diffraction data were collected using the one-dimensional silicon-based position-sensitive detector MYTHEN in Debye–Scherrer geometry in the 2θ angular range of 2–55° (0.7–15 Å d -range). The wavelength was set at $\lambda = 0.6194 \text{ \AA}$, calibrated using a Si NIST standard sample. The acquisition time was 5 min. Because the MYTHEN detector spans a $\approx 40^\circ$ angular 2θ range, this setup allows fast data acquisition with excellent statistics and high angular resolution. The instrumental contribution to the peak broadening was obtained by measuring a $\text{Na}_2\text{Ca}_3\text{Al}_2\text{F}_{14}$ (NAC) sample as line broadening reference.

Neutron diffraction was carried out on the sample with 4% nominal Ga content. The powder was put in a 6.5 mm diameter cylindrical vanadium sample holder and measured at $\lambda = 1.594 \text{ \AA}$



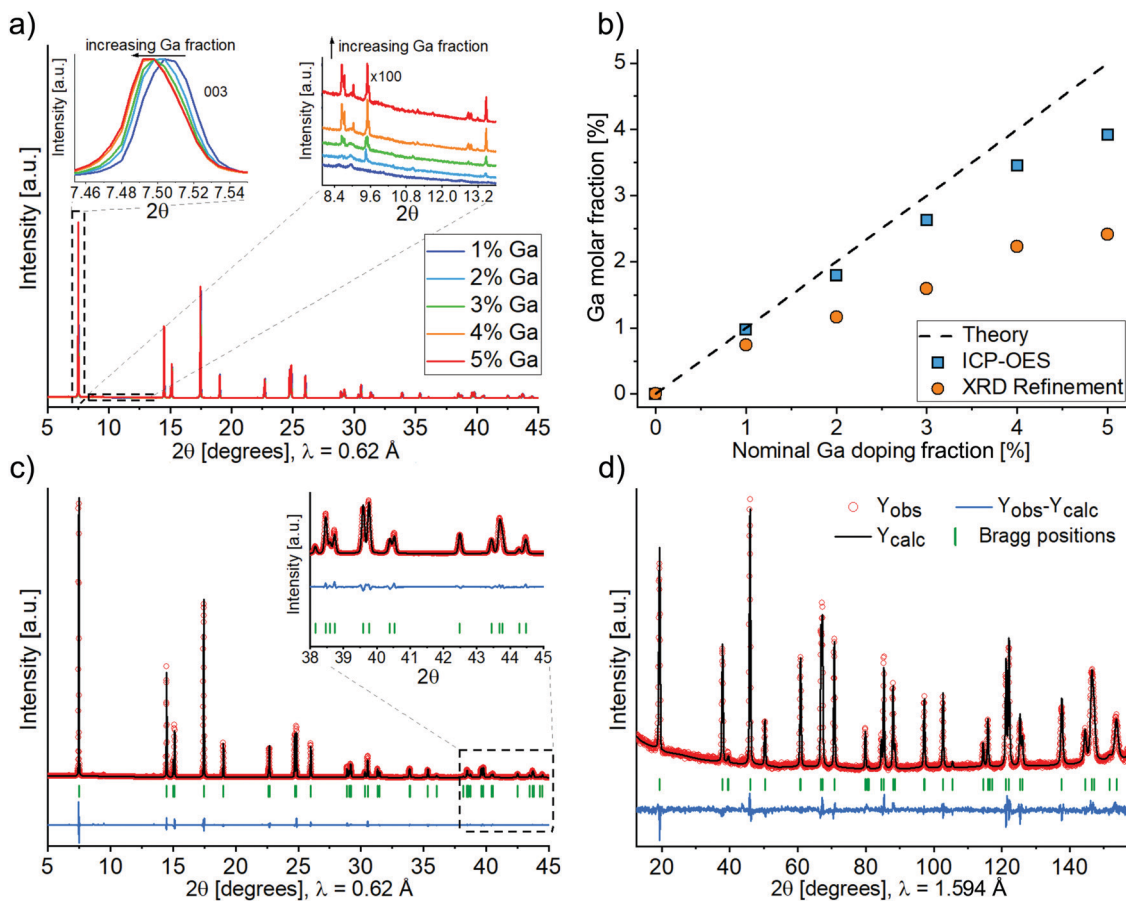


Fig. 2 (a) Synchrotron-based XRD patterns of LNO samples with 1 to 5 mol% nominal doping, normalized with respect to the 003 reflection intensity. The insets are zoomed-in views of the 2θ -ranges from 7.45 to 7.55° (left) and 8.3 to 13.4° (right), showing a shift in the 003 reflection position and the increasing amount of Li_5GaO_4 impurity with increasing Ga content, respectively. (b) Total Ga molar fraction of samples as function of the nominal doping fraction, as determined by ICP-OES and by Rietveld refinement of the XRD data (Ga fraction (site occupancy factor) in the Li layer (3b site) of the layered structure). The Ga fraction is derived from ICP-OES data considering the stoichiometry $\text{Li}_{1-y}\text{Ga}_y\text{NiO}_2$ and neglecting impurity phases. (c and d) Combined refinement of synchrotron-based X-ray (c) and neutron (d) diffraction patterns of Ga-doped LNO (4% nominal doping). Inset: Zoomed-in view of the 2θ -range from 38° to 45°.

The former step is known to promote hydroxide decomposition and an initial lithiation of the rock salt-type structure,²⁵ while the latter represents an optimum temperature for synthesis of well-oxidized and well-crystallized LNO, avoiding excessive decomposition of the material.^{3,8}

Fig. 1a and b show representative SEM images of as-synthesized Ga-doped LNO. All samples, including the reference LNO, exhibit comparable secondary particle morphologies. Typically, the secondary particles are of spherical shape, the majority having diameters in the range between 6 and 9 μm . However, smaller spherical secondary particles and larger agglomerates (mostly in the size range of 10–14 μm) are present as well. The primary particles size is found to be quite variable, ranging between 100 and 600 nm. Fig. 1c depicts primary particles at higher magnification, as captured during STEM investigation of the pristine sample. Fig. 1d and e shows STEM-EDX images of the respective area. A nearly uniform Ga signal originating from the primary particles indicates the homogeneous distribution of Ga into the structure of LNO.

The crystal structure of all samples was investigated by synchrotron-based X-ray diffraction (Fig. 2a). The diffraction patterns vary only slightly between different samples, as can be

seen from the insets in Fig. 2a. The angular shift of Bragg reflections towards smaller angles with increasing Ga content indicates firstly that doping was achieved and secondly that Ga enlarges the unit cell parameter of LNO. A small but increasing amount of the impurity phase Li_5GaO_4 (ICSD 9082) was observed with increasing amount of Ga precursor. Fig. 2b shows the total Ga content of the synthesized samples, which was determined by ICP-OES. According to ICP-OES, the nominal doping ranges from 0 to 4%, most likely due to an underestimated water content of the precursor $\text{Ga}(\text{NiO}_3)_3 \cdot x\text{H}_2\text{O}$ (despite the fact that x was determined by thermogravimetric analysis, see Fig. S1, ESI†). Furthermore, Fig. 2b includes the content of Ga ions in the Li layer (site occupancy factor of the 3b site), as determined by Rietveld refinement of XRD data (details of the refinement are discussed in the following). The actual Ga content was lower than the ICP-OES values, which can be mainly accounted for by the formation of the impurity phase Li_5GaO_4 . While its presence was negligible in case of 1–2% nominal doping, Rietveld analysis of the powder XRD data yielded estimated fractions of Li_5GaO_4 of 0.5, 0.8 and 0.9 mol% in the samples with 3, 4 and 5% nominal doping, respectively. This indicates a



In summary, we found that the Ga^{3+} ion takes the role of off-stoichiometric Ni^{2+} which is usually found in the Li layer in LNO ($[\text{Li}_{1-z}\text{Ni}_z]\text{NiO}_2$). One should note that, as previously mentioned, the ionic size of Ga^{3+} is larger than the size of Ni^{3+} constituting the Ni layers, while it is smaller than the size of Ni^{2+} and Li^+ , usually occupying the Li interlayer. So both locations are equally likely. Moreover, Ga^{3+} is more effective than Ni^{2+} at reducing the average Ni oxidation state in the sample, thus facilitating its synthesis.

Fig. 3 shows the evolution of lattice parameters with increasing Ga content. Both a and c parameters increase upon Ga incorporation, as expected from the shift of the Bragg reflections (Fig. 2a). Consequently, the unit cell volume increases as well. This effect decreases as the Ga content gets higher, *i.e.*, the relation is not linear over the investigated doping range. The ca ratio fluctuates around the value of our reference LNO (4.9383), however, with small relative changes. An approximately constant ratio is also reported in the literature.⁴ This indicates that the extent of rhombohedral distortion is neither improved nor worsened by the presence of Ga, as opposed to other dopants such as Co that typically stabilize the layered structure of LNO (namely they increase the amount of rhombohedral distortion of the original cubic lattice).²⁸

Fig. 4 shows the z -coordinate of the oxygen atom in LNO. A slight reduction of z can be noticed with increasing Ga fraction in the structure. The interlayer thickness $I = c/3 - S$ (where c is the unit cell parameter and S represents the Ni layer thickness) decreases with increasing Ga content, which is consistent with Ga being inserted into the Li layer (due to the smaller ionic

radius of Ga^{3+} compared to Li^+). In contrast, the layer thickness $S = c(2/3 - 2z_{\text{ox}})$ increases, which can be explained by the partial reduction of Ni^{3+} to Ni^{2+} to maintain charge neutrality. As a trivalent Ga ion substitutes a monovalent Li ion, two Ni^{3+} ions are reduced to Ni^{2+} according to $\text{Li}_{1-y}\text{Ga}_y[\text{Ni}^{3+}_{1-2y}\text{Ni}^{2+}_{2y}]\text{O}_2$.

Then, the electrochemical performance of the Ga-doped LNO CAMs was tested. Fig. 5a shows the first cycle voltage profiles of the different samples. The initial specific charge and discharge capacities decreased with increasing Ga content, as expected due to the redox inactivity of gallium. However, the big differences between the initial capacities can partly be

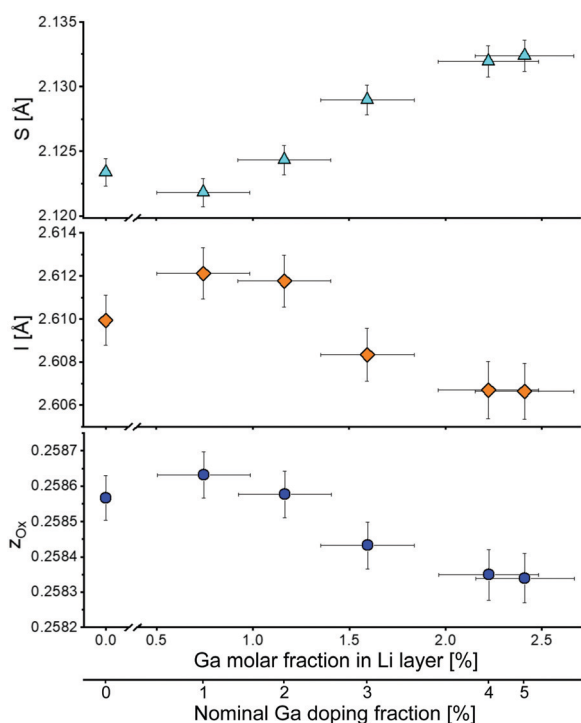


Fig. 4 Layer thickness S , interlayer thickness I and z -coordinate of oxygen z_{ox} as a function of the Ga content in the Li layer. The bottom x-axis indicates the nominal Ga doping.

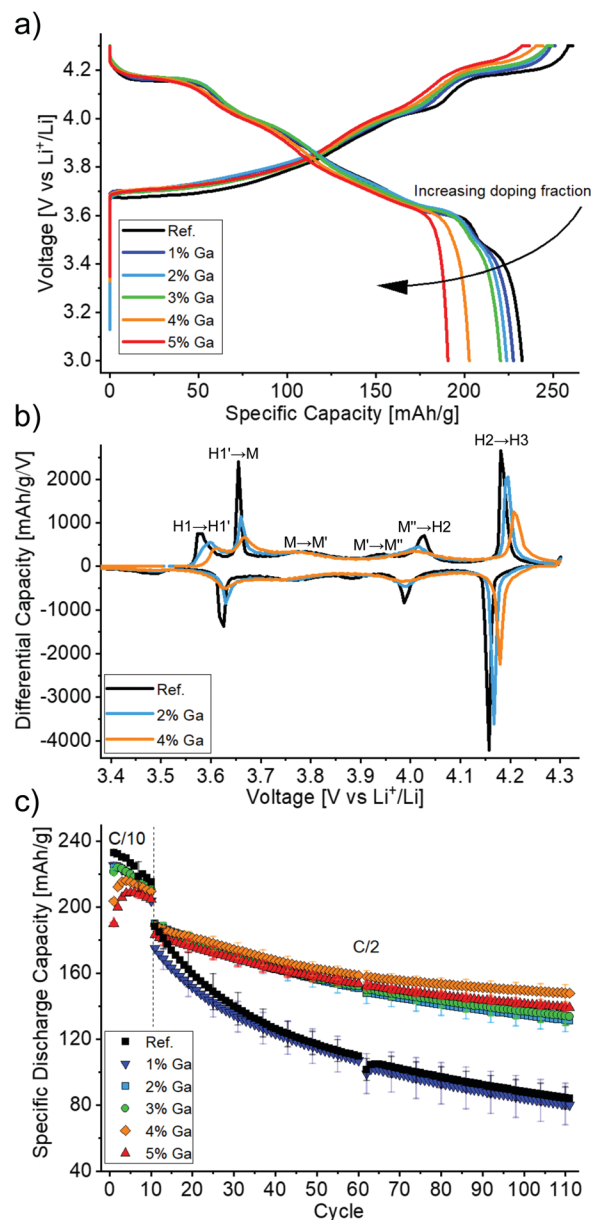


Fig. 5 Electrochemical data for undoped and Ga-doped LNO from galvanostatic cycling of half-cells at 25 °C in the voltage range between 3.0 and 4.3 V vs. Li^+/Li . (a) 1st cycle voltage profiles. (b) 3rd cycle differential capacity plots. Only selected samples are shown for clarity. (c) Specific discharge capacity over 110 cycles.



explained by the initial capacity activation period (*i.e.*, the largest capacities are not reached in the first cycle), which may last for 2 to 5 cycles. This initial increase in capacity is more pronounced for 4 and 5% nominal doping and is presumably a surface-related phenomenon, which is beyond the scope of this work. Furthermore, the voltage profiles show less pronounced plateaus and more sloped curves for higher Ga contents. This suggests a more solid solution-like behavior caused by the doping, which is in line with findings in the literature.^{19,22}

The trend towards solid solution-like behavior becomes even more apparent in the third cycle differential capacity plots (Fig. 5b). One can notice the typically observed sequence H1 → M → H2 → H3 (with H and M denoting hexagonal and monoclinic phases, respectively) with transitions at around 3.65, 4.0 and 4.2 V during charging. Additionally, H1 → H1', M → M' and M' → M'' represent transitions that were ascribed to Li vacancy ordering processes.^{8,9} As expected from the voltage plateaus in the charge/discharge curves above, all observed features are most pronounced for LNO. In contrast, the peak intensities are consistently diminished both in charge and discharge with increasing Ga content. Notably, the broad peaks between 3.75 and 3.80 V as well as between 3.87 and 3.95 V *vs.* Li⁺/Li (charge) in the monoclinic domain of the reference LNO sample were almost completely suppressed for the doped samples.

Interestingly, one may also note from Fig. 5b that the average voltage of most of the features is increased for higher Ga contents. This occurs both in charge and discharge, so it does not indicate an increased polarization but rather a true thermodynamic increase in the equilibrium (de)intercalation voltage. Such an effect has been already reported for doping with Al and related to the different nature of the Al–O bond as opposed to the transition metal–oxygen bond. In the former, a higher voltage is required to extract electrons from orbitals of

mostly anionic character, thus strongly influencing the voltage curve.^{29–31} Of note, an increased polarization in Al-doped LNO (for 10–50% substitution of Ni) has been reported and related to hindered charge delocalization in the Ni layer.³² Here, we did not observe higher polarization for increased Ga contents.

LNO with a nominal Ga content of 4% (2.2% as determined by Rietveld refinement), exhibited the largest specific discharge capacities after 110 cycles with a retention of 78% (Fig. 5c). For all nominal doping levels, except 1% Ga, significantly improved cycling performance was achieved with respect to the reference LNO. The respective values for the other samples of the doping series ranged between 69 and 76% (compared to 45 and 46% for the reference LNO and the 1% nominal doping, respectively). It should be noted that our reference LNO was not prepared under “optimal” LNO synthesis conditions, but instead it underwent the same treatment steps (wet-mixing, pre-annealing) as the doped samples. It is apparent that the synthesis approach chosen here has adverse effects on the capacity retention of the LNO reference CAM. While its initial specific discharge capacity was high (230 mA h g⁻¹), better capacity retention can well be achieved for undoped LNO.⁶

The 2.2% Ga doping of the best material is in line with the optimal doping levels for Ga reported in the literature.^{19,22} It appears that this optimum represents a compromise between structural stabilization and formation of impurity phases. However, the high retention of 95% after 100 cycles reported by Nishida *et al.*¹⁹ could not be reproduced. Of note, these values were obtained at a rate of about 0.19C with 8 h of CV charging at 4.3 V, which is a rather unpractical cycling protocol and presumably the reason for a capacity increase from initially 190 to 200 mA h g⁻¹ in the 60th cycle.

Operando XRD on the best-performing CAM was carried out to clarify the behavior of Ga-doped LNO during the (de)intercalation of lithium upon electrochemical cycling. This is the first

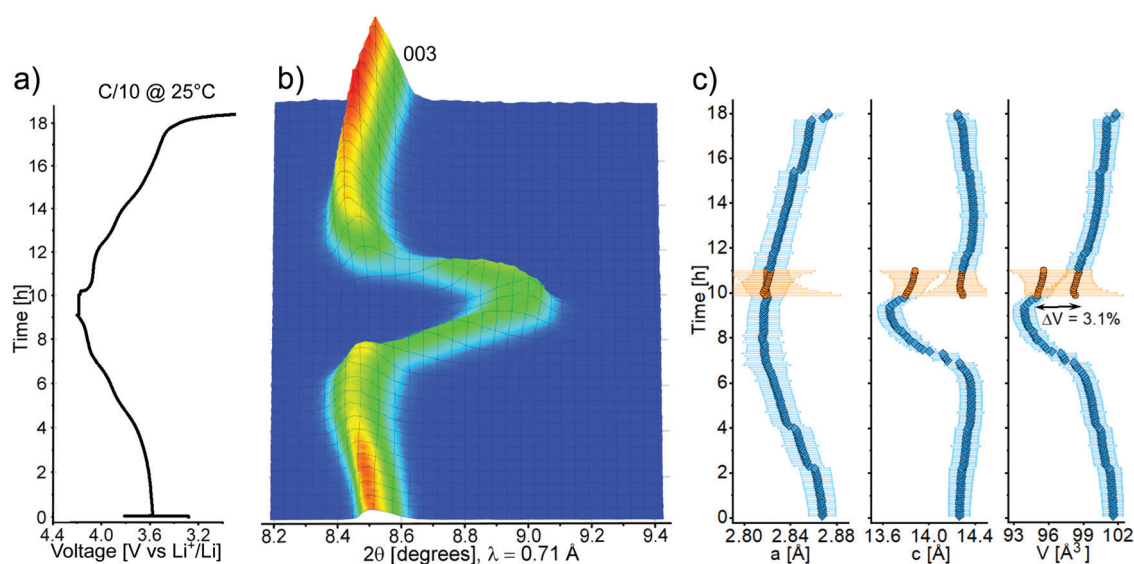


Fig. 6 (a) Voltage profile during *operando* XRD of a half-cell containing doped LNO (2.2% actual Ga content) cycled between 3.0 and 4.3 V *vs.* Li⁺/Li. (b) Contour plot showing the evolution of the 003 reflection. (c) Corresponding variation of the lattice parameters *a* and *c* and the unit cell volume *V*. Blue squares and orange circles denote monophasic and biphasic regions, respectively.



synchrotron-based XRD. In contrast to previous reports, the dopant was found to be most likely localized in the Li layer of the host structure based on combined Rietveld refinement of synchrotron-based XRD and neutron diffraction data. As a consequence, the extent of the adverse off-stoichiometry of LNO, *i.e.*, the presence of Ni ions in the interlayer, was reduced. Furthermore, with increasing dopant fraction, increasing lattice parameters, unit cell volume and layer thickness as well as decreasing interlayer distance ensued. While reducing the initial specific capacity, Ga incorporation improved the capacity retention over 110 cycles, with the best results at 2.2 mol% Ga doping, similar to previously reported optimal fractions. *Operando* XRD revealed an asymmetric behavior for the structural transition of the Ga-doped LNO between charge and discharge, indicating solid solution-like behavior during Li deintercalation (charge) and biphasic behavior for Li intercalation (discharge). The large overall volume change upon cycling was reduced by Ga doping, notably thanks to a smoother H2–H3 transition. *Ex situ* STEM analysis revealed that problems like mechanical instability and the formation of a surface rock salt layer still persist in Ga-doped LNO and are likely the main reasons for capacity fading. Overall, Ga is an effective dopant for LNO although its use alone is not sufficient to fully stabilize the material, which still requires further improvement, in particular of its surface properties.

Conflicts of interest

There are no conflicts to declare.

Acknowledgements

This study is part of the projects being supported by BASF SE. The work was partly performed with the support of the Karlsruhe Nano Micro Facility (KNMF), a Helmholtz Research Infrastructure at Karlsruhe Institute of Technology (KIT). We thank Dr. Thomas Bergfeldt (Institute for Applied Materials, IAM, KIT) for ICP-OES measurements.

References

- D. Andre, S. J. Kim, P. Lamp, S. F. Lux, F. Maglia, O. Paschos and B. Stiaszny, *J. Mater. Chem. A*, 2015, **3**, 6709–6732.
- J. R. Dahn and C. A. Michal, *Solid State Ionics*, 1990, **44**, 87–97.
- T. Ohzuku, A. Ueda and M. Nagayama, *J. Electrochem. Soc.*, 1993, **140**, 1862–1870.
- M. Bianchini, M. Roca-Ayats, P. Hartmann, T. Brezesinski and J. Janek, *Angew. Chem., Int. Ed.*, 2019, **58**, 10434–10458.
- A. Rougier, P. Gravereau and C. Delmas, *J. Electrochem. Soc.*, 1996, **143**, 1168–1175.
- C. S. Yoon, D. W. Jun, S. T. Myung and Y. K. Sun, *ACS Energy Lett.*, 2017, **2**, 1150–1155.
- M. Guilmard, C. Poullierie, L. Croguennec and C. Delmas, *Solid State Ionics*, 2003, **160**, 39–50.
- H. Li, N. Zhang, J. Li and J. R. Dahn, *J. Electrochem. Soc.*, 2018, **165**, A2985–A2993.
- L. de Biasi, A. Schiele, M. Roca-Ayats, G. Garcia, T. Brezesinski, P. Hartmann and J. Janek, *ChemSusChem*, 2019, **12**, 2240–2250.
- H. K. T. Ohzuku, A. Ueda, M. Nagayama and Y. Iwahoshi, *Electrochim. Acta*, 1993, **38**, 1159–1167.
- E. Rossen, C. D. W. Jones and J. R. Dahn, *Solid State Ionics*, 1992, **57**, 311–318.
- M. Guilmard, A. Rougier, M. Grüne, L. Croguennec and C. Delmas, *J. Power Sources*, 2003, **115**, 305–314.
- H. Arai, M. Tsuda and Y. Sakurai, *J. Power Sources*, 2000, **90**, 76–81.
- C. Poullierie, L. Croguennec, P. Biensan, P. Willmann and C. Delmas, *J. Electrochem. Soc.*, 2000, **147**, 2061–2069.
- H. Li, M. Cormier, N. Zhang, J. Inglis, J. Li and J. R. Dahn, *J. Electrochem. Soc.*, 2019, **166**, A429–A439.
- U. H. Kim, D. W. Jun, K. J. Park, Q. Zhang, P. Kaghazchi, D. Aurbach, D. T. Major, G. Goobes, M. Dixit, N. Leifer, C. M. Wang, P. Yan, D. Ahn, K. H. Kim, C. S. Yoon and Y. K. Sun, *Energy Environ. Sci.*, 2018, **11**, 1271–1279.
- H. H. Ryu, G. T. Park, C. S. Yoon and Y. K. Sun, *J. Mater. Chem. A*, 2019, **7**, 18580–18588.
- C. S. Yoon, U. H. Kim, G. T. Park, S. J. Kim, K. H. Kim, J. Kim and Y. K. Sun, *ACS Energy Lett.*, 2018, **3**, 1634–1639.
- Y. Nishida, K. Nakane and T. Satoh, *J. Power Sources*, 1997, **68**, 561–564.
- M. Y. Song, C. K. Park, S. Do Yoon, H. R. Park and D. R. Mumm, *Ceram. Int.*, 2009, **35**, 1145–1150.
- M. Song, S. Kwon, I. Kwon and H. Park, *J. Appl. Electrochem.*, 2007, **37**, 421–427.
- S. N. Kwon, D. R. Mumm, H. R. Park and M. Y. Song, *J. Ceram. Process. Res.*, 2016, **17**, 653–658.
- R. D. Shannon, *Acta Crystallogr., Sect. A: Cryst. Phys., Diffraction, Theor. Gen. Crystallogr.*, 1976, **32**, 751–767.
- F. Fauth, I. Peral, C. Popescu and M. Knapp, *Powder Diffraction*, 2013, **28**, S360–S370.
- M. Bianchini, F. Fauth, P. Hartmann, T. Brezesinski and J. Janek, *J. Mater. Chem. A*, 2020, **8**, 1808–1820.
- H. Liu, H. Liu, S. H. Lapidus, Y. S. Meng, P. J. Chupas and K. W. Chapman, *J. Electrochem. Soc.*, 2017, **164**, A1802–A1811.
- C. Poullierie, E. Suard and C. Delmas, *J. Solid State Chem.*, 2001, **158**, 187–197.
- D. Caurant, N. Baffier, B. Garcia and J. P. Pereira-Ramos, *Solid State Ionics*, 1996, **91**, 45–54.
- M. Aydinol, A. Kohan, G. Ceder, K. Cho and J. Joannopoulos, *Phys. Rev. B: Condens. Matter Mater. Phys.*, 1997, **56**, 1354–1365.
- G. Ceder, Y. M. Chiang, D. R. Sadoway, M. K. Aydinol, Y. I. Jang and B. Huang, *Nature*, 1998, **392**, 694–696.
- Y. Il Jang, B. Huang, H. Wang, G. R. Maskaly, G. Ceder, D. R. Sadoway, Y. M. Chiang, H. Liu and H. Tamura, *J. Power Sources*, 1999, **81–82**, 589–593.
- M. Guilmard, L. Croguennec, D. Denux and C. Delmas, *Chem. Mater.*, 2003, **15**, 4476–4483.
- L. Mu, R. Zhang, W. H. Kan, Y. Zhang, L. Li, C. Kuai, B. Zydlewski, M. M. Rahman, C. J. Sun, S. Sainio, M. Avdeev, D. Nordlund, H. L. Xin and F. Lin, *Chem. Mater.*, 2019, **31**, 9769–9776.

